Materials Advances

ROYAL SOCIETY OF CHEMISTRY

PAPER

View Article Online
View Journal | View Issue

Cite this: *Mater. Adv.*, 2023, 4, 1998

Hierarchical cathode constructed by carbon coated $Na_{3.5}VMn_{0.5}Cr_{0.5}(PO_4)_3$ nanoparticles on rGO for high-capacity and long-cycle life sodium storage†

Jinhao Wang, Longzhu Zhao and Fengqi Lu *

Received 16th February 2023,
Accepted 28th March 2023

DOI: 10.1039/d3ma00074e

rsc.li/materials-advances

Mn-substituted NASICON-type $Na_{3+x}Mn_xV_{2-x}(PO_4)_3$ compounds have been extensively studied as desirable cathode materials for sodium-ion batteries (SIBs) due to their higher operating voltage, low cost and weak biological toxicity compared with $Na_3V_2(PO_4)_3$. However, they present limited reversible capacity and cycling properties originating from the low electronic conductivity and irreversible phase transition caused by the Jahn–Teller active Mn^{3+}. Herein, the electronic conductivity and structural stability of the material are ameliorated by constructing a double-carbon-layer hierarchical structure and substitution of Mn by Cr. As expected, the unique hierarchical $Na_{3.5}VMn_{0.5}Cr_{0.5}(PO_4)_3$@C/rGO electrode demonstrates excellent sodium-ion storage properties, consisting of a 2.4-electron redox reaction, high energy density (472 W h kg^{-1}), cycling performance with 94.7% capacity retention after 1600 cycles at 10C, along with a retention of 81% after 8000 cycles at 20C. Moreover, the full cell based on the $Na_{3.5}VMn_{0.5}Cr_{0.5}(PO_4)_3$@C/rGO cathode and hard carbon anode demonstrates a reversible capacity of 119 mA h g^{-1} with an energy density of 405.8 W h kg^{-1} at 0.2C, and a high capacity retention ratio of 94.6% at 1C after 200 cycles. Such dual-carbon hierarchical engineering will facilitate the application of NASICON-type cathodes in sodium ion batteries for grid-scale energy storage systems.

Introduction

Sodium-ion batteries (SIBs) are considered to be ideal contenders for grid-scale stationary energy storage devices.[1–5] To date, hard carbon (HC) may be the most suitable candidate anode for SIBs, owing to its low cost and abundance.[6,7] As a key component, the properties of the cathode have a significant effect on the total performance of the battery.[8–11] However, bottlenecks still exist in the energy density and cyclability of cathode materials.[12–15] Thus, enhancing the cathode material working voltage, practical capacities and cyclability remain a critical prerequisite to design high-performance SIBs. However, there are still enormous challenges to overcome these bottlenecks.[16] Various types of compounds, including transition-metal oxides, Prussian blue analogs and polyanion compounds, have been extensively investigated as cathode materials for SIBs.[17–22] Among these material candidates, $Na_3V_2(PO_4)_3$, which belongs to polyanion compounds with a Na super ionic conductor (NASICON) structure, has great potential for application in SIBs owing to its high operating voltage, open framework for facilitating Na ion mobility, thermodynamic stability and high safety.[23–29]

Regrettably, it faces extreme constrictions owing to limited vanadium (V) abundance, relatively high cost and high biological toxicity. To reduce the content of V and toxicity, as well as increase the energy density and operating voltage, various transition metal ions, such as Mn^{2+}, Fe^{2+}/Fe^{3+}, Cr^{3+}, Ti^{4+} and Zr^{4+}, are used to replace V^{3+}.[30–38] In 2016, Goodenough reported on the use of $Na_xMV(PO_4)_3$ (M = Mn, Fe, Ni) to enhance the working potential of the cathode by the modification of V^{4+}/V^{3+}, Mn^{3+}/Mn^{2+}, and Fe^{3+}/Fe^{2+} redox centers.[39] Afterwards, the $Na_4MnCr(PO_4)_3$/C cathode was prepared and displayed a high output potential of about 3.53 V and a three-electron reaction (Mn^{2+}/Mn^{3+}, Mn^{3+}/Mn^{4+} and Cr^{3+}/Cr^{4+} couples) presenting a high specific energy of about 566 W h kg^{-1}.[40] Lavela *et al.* unveiled the effect of Cr substitution to enhance the behavior of $Na_4MnV(PO_4)_3$ at high voltages and improve sodium diffusivity, leading to a net gain in the reversible extraction and low interface resistance for high substitution content (>0.6).[41] Nevertheless, the cycling stabilities of Mn-based NASICON-type cathodes are sacrificed because the Jahn–Teller effect of

Key Laboratory of New Processing Technology for Nonferrous Metal & Materials Ministry of Education, Guangxi Key Laboratory of Optical and Electronic Materials and Devices, College of Materials Science and Engineering, Guilin University of Technology, Guilin, 541004, P. R. China. E-mail: lufengqi@glut.edu.cn

† Electronic supplementary information (ESI) available. See DOI: https://doi.org/10.1039/d3ma00074e

Mn(III) seems to be inevitable during the whole reaction. Therefore, it is highly desirable but remains a big challenge to further develop a synergic strategy to inhibit the Jahn–Teller effect and improve the cycling durability of Mn-based NASICON-type cathodes.

Herein, we investigate the effects of Cr ion substitution on the crystal structure distortion and electrochemical performance of the NASICON-type $Na_{3.5}VMn_{0.5}Cr_{0.5}(PO_4)_3$ cathode. A hierarchical structure incorporated with a double-carbon strategy is utilized to enhance the electronic conductivity and conductivity/ionic diffusion capability. As a result, the as-prepared $Na_{3.5}VMn_{0.5}Cr_{0.5}(PO_4)_3$@C/rGO demonstrates a 2.4-electron redox reaction from V^{3+}/V^{4+}, Mn^{2+}/Mn^{3+} and V^{4+}/V^{5+} redox couples, leading to a high reversible capacity (136 mA h g^{-1} at 0.2C and 75.8 mA h g^{-1} at 20C) and high cycling retention (94.7% after 1600 cycles at 10C and 81% after 8000 cycles at 20C). Benefiting from the excellent electrochemical properties of VMC@C/rGO, the VMC@C/rGO//HC full cell realizes a desired energy density of 405.8 W h kg^{-1}. This hierarchical engineering will shed light on the reasonable construction of a NASICON-structural cathode with high-energy for SIBs.

Experimental

Sample synthesis

The hierarchical $Na_{3.5}VMn_{0.5}Cr_{0.5}(PO_4)_3$@C/rGO (VMC@C/rGO) composite was synthesized *via* a sol–gel route, followed by an annealing calcination (Scheme 1). Graphene oxide (GO) was firstly prepared by Hummers' method[42] and dispersed in deionized water under sonication. Next, CH_3COONa, $Mn(CH_3COO)_2{\cdot}4H_2O$, $Cr(CH_3COO)_3$, V_2O_5 and $NH_4H_2PO_4$ were mixed in 60 mL deionized water with the molar ratios corresponding to the target chemical formula at 60 °C for 2 h. After adding the graphene oxide solution, the mixed solution was dried under stirring at 90 °C to a gel and vacuum-dried overnight. Finally, the dried-precursor was calcined at 400 °C for 2 h, followed by 700 °C for 6 h in an Ar atmosphere to generate the VMC@C/rGO composite. As compared, the $Na_{3.5}VMn_{0.5}Cr_{0.5}(PO_4)_3$@C (VMC@C) sample was prepared using the same process without GO.

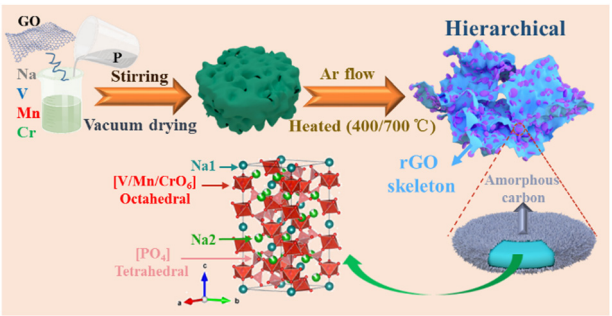

Scheme 1 Schematic diagram of preparation hierarchical VMC@C/rGO composite.

Sample characterization

The powder X-ray diffraction pattern (XRD) data were recorded by a PANalytical EMPYREAN X-Ray Diffractometer with Cu Kα radiation (1.5418 Å). Rietveld refinements were performed using TOPAS-Academic. A thermogravimetric analyzer (TG, STA8000) was used to determine the carbon and rGO contents. The morphologies and microstructures of the powder samples were characterized by scanning electron microscope (SEM, ZEISS Sigma) and transmission electron microscopy (TEM, JEM2010-HR). The Raman spectra were recorded using the Laser Micro-Raman Spectrometer DXR series. The surface area and the pore-size distributions of the samples were tested and calculated using nitrogen adsorption and desorption isotherm measurements (TriStar II 3020). The elemental compositions of the samples were characterized *via* inductively coupled plasma-optical emission spectroscopy (ICP-OES) analysis using a PerkinElmer Optima 8000 analyzer.

Electrochemical measurements

The working electrodes consisted of the active material, conductive carbon black, and polyvinylidene fluoride (PVDF) binder (7 : 2 : 1) to form the electrode slurry in *N*-methyl-2-pyrrolidone (NMP). The obtained slurry was coated on an Al foil, then dried under vacuum at 100 °C overnight. The mass loading of the active material was roughly 2 ± 0.2 mg cm^{-2}. The hard carbon (HC) electrode was prepared with the ratio of 8 : 1 : 1 by a similar process. Glass fiber (GF/D, Whatman) was used as the separator, and sodium metal was used as the counter electrode. Coin cells (CR2032) were assembled in a glove box filled with pure Ar and aged overnight before testing. The galvanostatic charge–discharge process and the galvanostatic intermittent titration technique (GITT) were carried out on a Neware battery test system (CT-4008T-5V10mA-164, Shenzhen Neware Co., Ltd, China). Cyclic voltammetry (CV) and (EIS) measurements were performed on an electrochemical workstation (CHI760E, Chenhua, Shanghai, China).

Results and discussions

The crystal structures of the as-synthesized VMC@C and VMC@C/rGO were characterized by X-ray diffraction (XRD) measurement, and the XRD data were refined by the Rietveld method (Topas V4 program). The refined results of the VMC@C and VMC@C/rGO samples are displayed in Fig. 1. The refinement reliability factors are shown in Table S1 (ESI†), and the detailed structural information of the atom positions and occupancies of VMC@C/rGO are exhibited in Table S2 (ESI†). Both VMC@C and VMC@C/rGO samples have a rhombohedral NASICON structure with the space group of $R\bar{3}c$. However, some new peaks are detected in VNM@C/rGO, which are characteristic of graphitized carbon. The refined lattice parameters of VMC@C/rGO are a = 8.8032(2) Å, c = 21.7323(7) Å, V = 1460.22(9) $Å^3$. V, Mn and Cr atoms are located at the same site of 12c. The V/Mn/CrO_6 octahedra and PO_4 tetrahedra share common O corners to build a robust 3D framework. Both sodium sites,

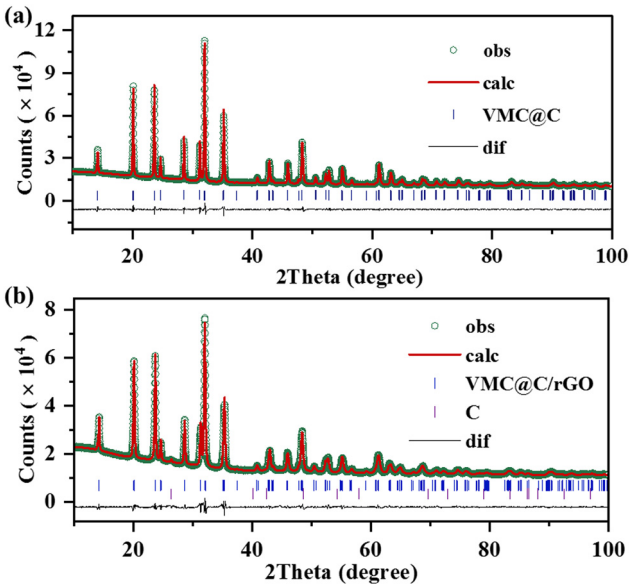

Fig. 1 XRD patterns with Rietveld refinement: (a) VMC@C, (b) VMC@C/rGO.

six-fold coordinated Na1 (6b) and eight-fold coordinated Na2 (18e), are occupied with the occupancy of 1 and 0.855, respectively, further confirming the stoichiometry of $Na_{3.5}VMn_{0.5}Cr_{0.5}(PO_4)_3$.

The morphologies of VMC@C and VMC@C/rGO were observed by SEM. The SEM image in Fig. 2a shows that the particles comprising the VMC@C samples assemble together with irregularity in shapes ranging from 200 to 500 nm. Fig. 2b and c reveals that the VMC@C particles are independent particles and tightly attach onto the surface of rGO in the VMC@C/rGO composite. This special hierarchical structure matrix could offer 3D pathways for fast electronic conductivity.[43] The microstructure of VMC@C/rGO was further characterized by TEM. The TEM images (Fig. 2d and Fig. S1, ESI†) reveal that VMC particles with 200–400 nm scale are embedded in the carbon matrix. Such a composite architecture could guarantee the facilitated reaction kinetics involved in fast Na ion migration and favorable electron conduction. Furthermore, the (HRTEM) image (Fig. 2e) presents that the exterior surface of the $Na_{3.5}VMn_{0.5}Cr_{0.5}(PO_4)_3$ particle is coated with a thin amorphous carbon layer (about 2.5 nm), which is derived from the pyrolysis of citric acid. Two distinguishable interplanar spacings of 0.62 nm and 0.37 nm match well with the $(10\bar{2})$ and $(2\bar{1}3)$ planes of the trigonal NASICON structure, respectively. The typical NASICON rhombohedral structure of VMC@C/rGO was further confirmed by SAED plot (Fig. 2f), which also indicates a high crystallinity of the as-prepared VMC@C/rGO compound. The EDS mapping images (Fig. 2g–m) show that the Na, V, Mn, Cr, P, O, and C elements are uniformly distributed in

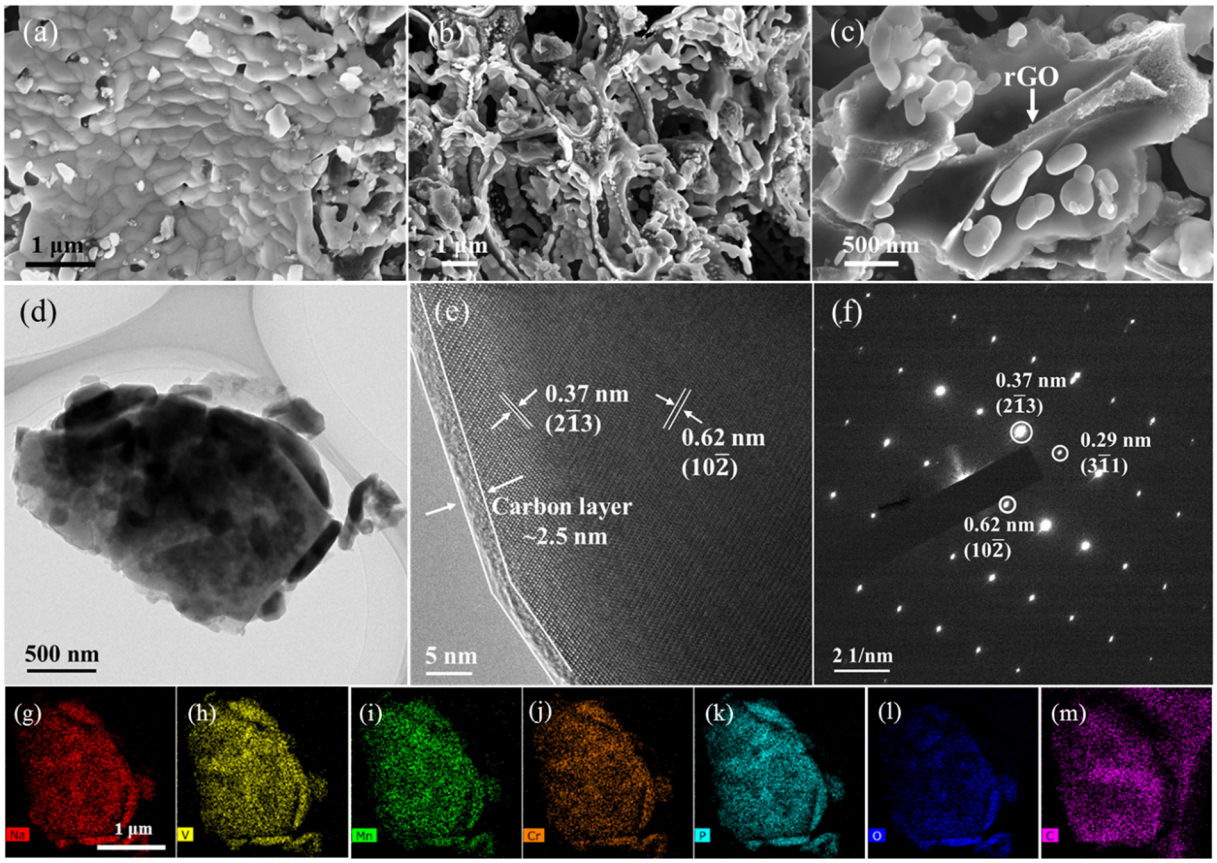

Fig. 2 (a) SEM image of VMC@C. (b and c) SEM images, (d) TEM image, (e) HR-TEM image, (f) SAED plot, (g–m) elemental mappings of Na (g), V (h), Mn (i), Cr (j), P (k), O (l), and C (m) of VMC@C/rGO.

the particles. The ratio of the Na : V : Mn : Cr metal elementals was determined to be 3.55 : 1 : 0.5 : 0.49 by ICP-OES analysis, which is consistent with the designed stoichiometric ratio of the $Na_{3.5}VMn_{0.5}Cr_{0.5}(PO_4)_3$ composition.

The carbon contents of the VMC@C and VMC@C/rGO samples are calculated as 12.8% and 15.4% by thermogravimetric analysis (Fig. S2, ESI†), respectively. Raman spectra (Fig. S3, ESI†) were used to research the nature of the carbon materials in VMC@C and VMC@C/rGO. Two broad peaks located at 1334 cm^{-1} and 1598 cm^{-1} can be ascribed to the D-band (defects in the graphite structure) and G-band (graphite carbon) of the carbon materials, respectively.[44–48] A high intensity ratio of the G-band and D-band for VMC@C/rGO (I_G/I_D = 1.13) indicates higher graphitized electronic conductivity than that of VMC@C (I_G/I_D = 0.98), which can be attributed to the highly graphitized rGO skeleton. Next, the nitrogen adsorption–desorption technique was utilized to characterize the specific surface area and pore structure of the composites (Fig. S4, ESI†). According to the Brunauer–Emmett–Teller (BET) method, the surface area of VMC@C/rGO is measured as 179 $m^2\ g^{-1}$, which is much higher than that of VMC@C (127 $m^2\ g^{-1}$). The Barrett–Joyner–Halenda (BJH) pore size distribution curves (the inset) reveal that the majority pore size in VMC@C and VMC@C/rGO are both about 4 nm. The high surface area and abundant pores are supposed to greatly enhance the high surface wettability, and result in a full utilization of the active material.

Electrochemical performances of the as-prepared cathodes were investigated by half coin-cells with sodium metal as anodes. The CV curves of VMC@C and VMC@C/rGO at a scan rate of 0.2 mV s^{-1} are shown in Fig. S5a (ESI†) and Fig. 3a. One couple of redox peaks in the CV curves of VMC@C and VMC@C/rGO centered at about 3.4/3.6 V are associated with the V^{3+}/V^{4+} and Mn^{2+}/Mn^{3+} redox couples, respectively. Moreover, there is a weak reversible redox peak of the V^{4+}/V^{5+} redox couple located at about 4 V in the VMC@C/rGO electrode,[49] which is verified by dQ/dV curve (inset of Fig. 3b) and absent in the VMC@C electrode. This phenomenon should be related to the conductance of the material. After innovation, the rGO conductive matrix in VMC@C/rGO can facilitate electron transfer, and the unique hierarchical structure can also shorten the migration path of Na^+ during the redox reaction, thereby triggering the partial oxidation of V^{4+} to V^{5+}.[43,50]

The rate capabilities of the VMC@C and VMC@C/rGO electrodes were characterized *via* galvanostatic testing at variable current densities from 0.2 to 20C in the voltage range of 2.0–4.2 V. In the charge–discharge profiles, both VMC@C (Fig. S5b, ESI†) and VMC@C/rGO (Fig. 3b) electrodes displayed similar correlative voltage plateaus with the above CV study. Three pairs of redox potentials at 3.42/3.53, 3.53/3.62, and 4.08/4.12 V are discovered in the dQ/dV plot of VMD@C/rGO (inset in Fig. 3b). The redox peaks correspond to the V^{3+}/V^{4+} and Mn^{2+}/Mn^{3+}, and V^{4+}/V^{5+} redox. Additionally, one irreversible oxidation peak is located at 4.11 V in the dQ/dV plot of VMC@C (inset of Fig. S5b, ESI†), which could be ascribed to the consumption of the electrolyte to yield the cathode electrolyte interphase (CEI) film.[51] The VMC@C/rGO displays the initial discharge capacity of 136 mA h g^{-1} with a working voltage of 3.47 V. This capacity corresponds to a 2.4-electron redox reaction per cell unit, which is larger than the transfer number of $Na_3V_2(PO_4)_3$.[52] Compared with VMC@C, the rate capability of VMC@C/rGO has greatly improved. The VMC@C/rGO electrode (Fig. 3c) can deliver a remarkable average revisable capacity of 122.4, 108.6, 101.6 94.6, 85.3 and 77.1 mA h g^{-1} from 0.2 to 10C. Even at the ultra-high rate of 20C, it is still able to display an average discharge capacity of 66.3 mA h g^{-1}. When the current density shifts to 0.2C from 20C, the reversible capacity returns to 108.3 mA h g^{-1}. However, VMC@C shows a much lower specific capacity under various current densities and only 55.3 mA h g^{-1} is obtained at 20C, indicating that the introduction of rGO is beneficial to the sodium storage capability of VMC@C/rGO. Moreover, the capacities of the electrodes slowly decay at the rate of 0.2C (Fig. 3c). This could be ascribed to the irreversible phase transition and the decomposition of the electrolyte to form the CEI film in the high voltage region,[41] which could be verified by electrochemical impedance spectroscopy (EIS).

Next, the cycling stability of the electrodes was also explored. As shown in Fig. 3d, VMC@C/rGO shows excellent long-term cycling stability at a high rate of 10C with a stable capacity of 78.5 mA h g^{-1} even after 1600 cycles, corresponding to the capacity retention of 94.7%. Impressively, Fig. 3e shows that the VMC@C/rGO sample can deliver an initial capacity of 75.8 mA h g^{-1} at the ultrahigh rate of 20C and maintains a remarkable capacity of 61.4 mA h g^{-1} after 8000 cycles with the capacity retention of 81%, corresponding to a decay percentage of 0.0024% per cycle. It should be noted that the electrode can retain a capacity retention of 90% over 3000 cycles. The latter performance after 5000 cycles demonstrates excellent cycling stability, with a capacity retention of 95.8%. Compared with other NASICON-type cathode materials (inset in Fig. 3e and Table S3, ESI†), VMC@C/rGO exhibits the most beneficial cyclic stability in long cycles, which is closely linked to the special hierarchical structure matrix modification by rGO.

To further verify the underlying reasons behind the improved electrochemical performances of the VMC@C/rGO electrode, GITT was conducted to compare the kinetic behaviors of the VMC@C and VMC@C/rGO electrodes. The D_{Na^+} of the VMC@C and VMC@C/rGO electrodes during the whole sodium insertion/extraction process were firstly characterized by GITT (Fig. S7, ESI†). During the GITT process, a current density of 0.1C was applied for 30 minutes to the electrode to control the Na-ion insertion and extraction, following by a relaxation process lasting for 120 minutes. The apparent Na-ion diffusion coefficient (D_{Na^+}) values were calculated using the equation:

$$D_{Na^+} = (4/\pi\tau)(m_B V_m)/(M_B S)^2(\Delta E_s)/(\Delta E_\tau)^2 \quad (\tau \le l^2/D) \qquad (1)$$

In (1), D_{Na^+} is the apparent Na-ion diffusion coefficient, τ is the relaxation time, and m_B, M_B, V_m, and S represent, the mass, molecular weight, molar volume and surface area of the cathode material, respectively. ΔE_s is the difference between

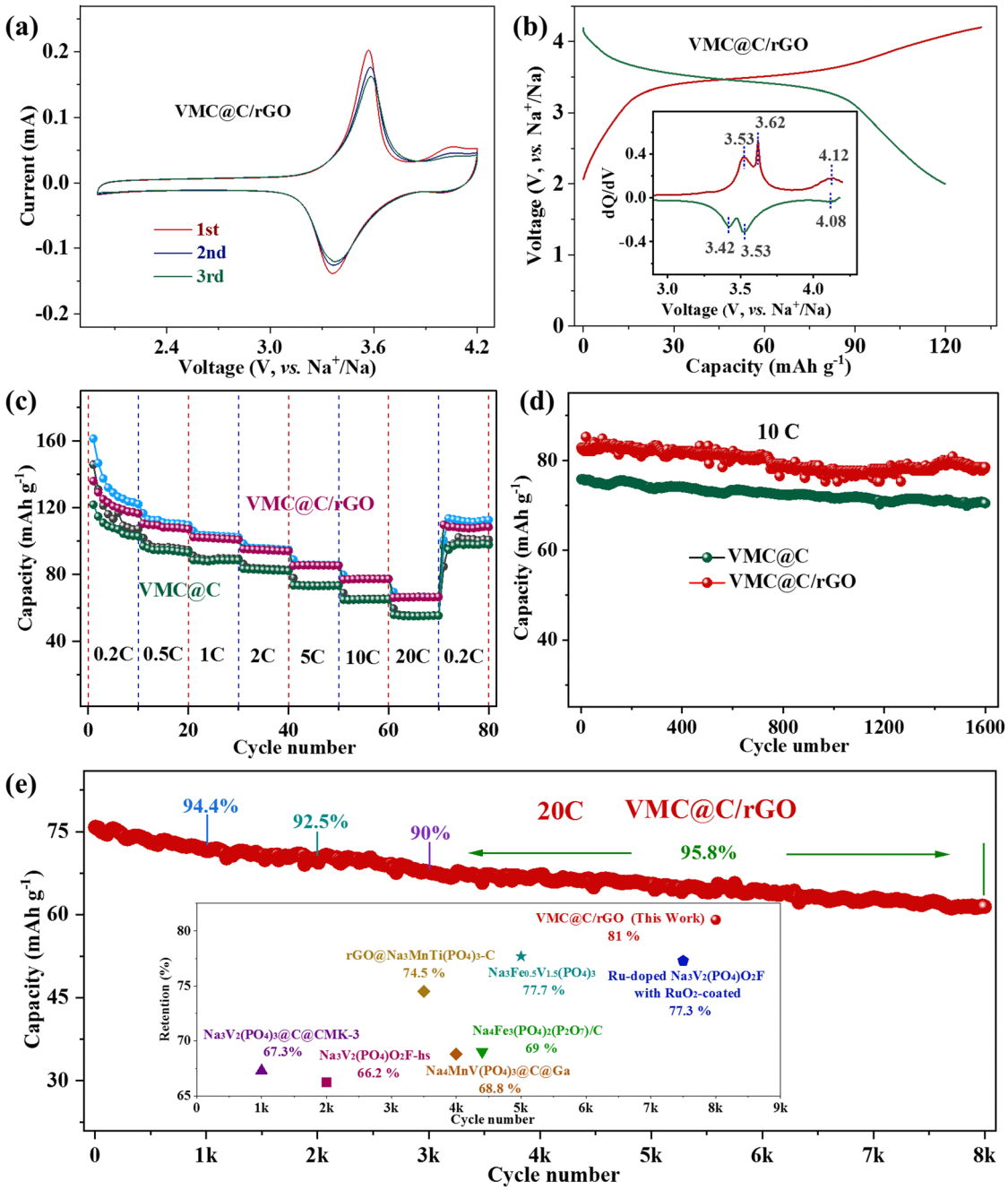

Fig. 3 Electrochemical properties of the VMC@C and VMC@C/rGO cathodes. (a) CV curves of VMC@C/rGO. (b) Charge/discharge profile of VMC@C/rGO at 0.2C; the inset is the corresponded dQ/dV plot. (c) Rate capabilities from 0.2 to 20C. (d) Cycling performance at 10C. (e) Cycling performance of VMC@C/rGO at the high rate of 20C; inset compared with the long cycling stability of other NASICON-type cathodes, $Na_3V_2(PO_4)_3$@C@CMK-3,[54] $Na_3V_2(PO_4)O_2F$-hs,[55] rGO@$Na_3MnTi(PO_4)_3$-C,[56] $Na_4MnV(PO_4)_3$@C@Ga,[57] $Na_4Fe_3(PO_4)_2(P_2O_7)$/C,[58] $Na_3Fe_{0.5}V_{1.5}(PO_4)_3$,[59] Ru-doped $Na_3V_2(PO_4)O_2F$ with RuO_2-coating.[60]

two consecutive stable voltages after relaxation. ΔE_τ is the transient change in voltage during a single titration step. The calculated results reveal that VMC@C/rGO holds higher D_{Na^+} than that of VMC@C, which fluctuates in the range of 10^{-13} to 10^{-11} cm^2 s^{-1}.

In general, there are two forms of charge storage behaviors toward an electrode material, one is a diffusion-controlled reaction, and the other one is the pseudo-capacitance. To expose the charge storage mechanism of the as-prepared samples, cyclic voltammetry (CV) curves were collected from 0.2 to 1 mV s^{-1}. As displayed in Fig. 4a and b, the slight shifting of the cathodic/anodic peaks and well-preserved CV shapes show the weak voltage polarization and excellent electrochemical reversibility. The diffusion-dominated and capacitive-controlled capacities can be quantitatively calculated from the CV data. The current response (I) at a fixed potential (V) can be

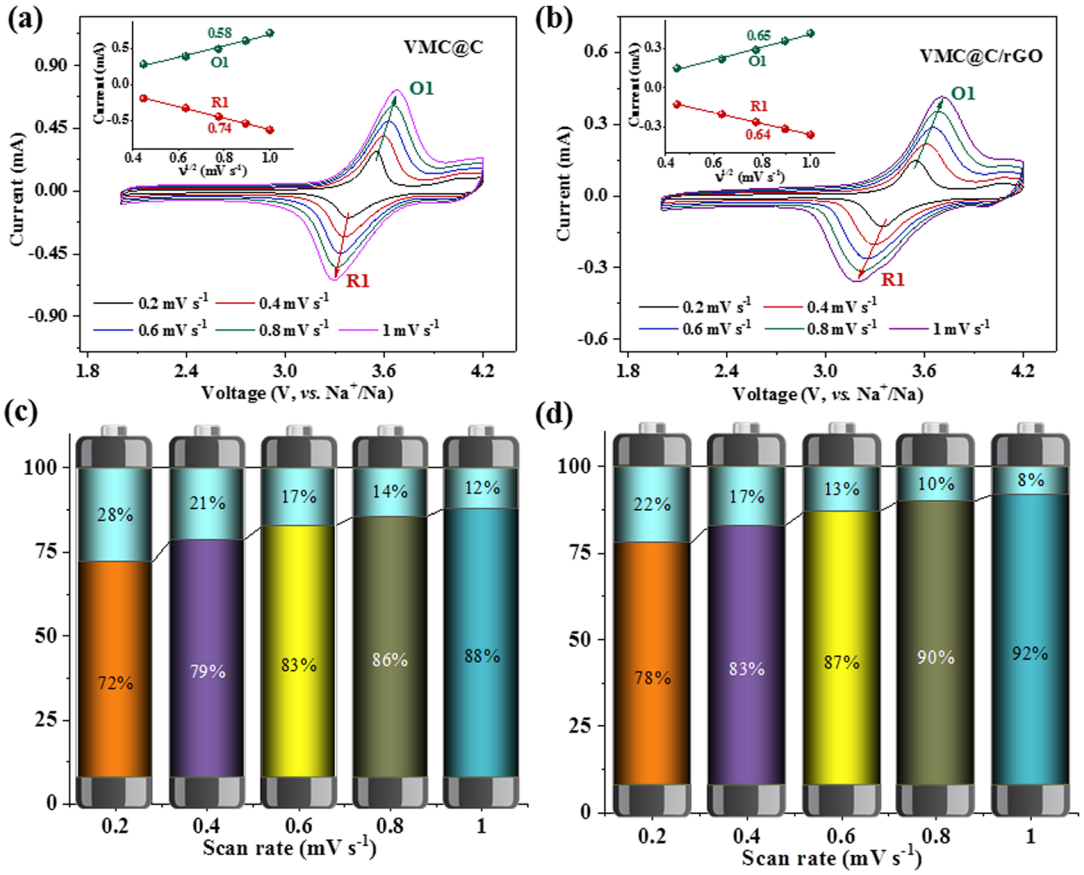

Fig. 4 CV curves of VMC@C (a) and VMC@C/rGO (b) for various scan rates; inset is the relationship between the peak current I_p and the square root of the scan rate $v^{1/2}$. Capacitive-controlled contributions for VMC@C (c) and VMC@C/rGO (d) at different scan rates.

described as a function of the scan rate (v), and the equation can be written as:[53]

$$I = av^b \quad (2)$$

$$I\,(\mathrm{V}) = k_1 v + k_2 v^{1/2} \quad (3)$$

where v is the scan rate. The k_1v component reflects the capacitive process and the $k_2v^{1/2}$ component reflects the controlled process. It is well known that the value of b approaching 0.5 indicates a diffusion-dominated electrochemical process, and the value of 1.0 demonstrates an electrochemical process controlled by the capacitive behavior. As displayed in the inset of Fig. 4a and b, the b values for the peaks of all the electrodes are above 0.5, indicating the existence of pseudo-capacitance behavior. The calculated proportion of pseudo-capacitance for VMC@C/rGO is depicted in Fig. 4c and d. Obviously, the VMC@C/rGO electrode shows relatively higher capacitive contribution values than the VMC@C electrode, which manifests improved cycling stability and rate capability.

Furthermore, the Na^+ diffusion coefficient (D_{Na^+}) can be calculated by the Randles–Sevcik equation based on the different CV scan rates.

$$I_p = 2.69 \times 10^5 n^{3/2} A C_o D^{1/2} \nu^{1/2} \quad (4)$$

where I_p and ν represent the peak current and scan rate, respectively. n is the number of electrons involved in the electrochemical reaction, A is the area of contact part between the cathode and electrolyte, C_o is the concentration of Na^+ in the electrode, and D is the apparent diffusion coefficient (D_{Na^+}). Apparently, the VMC@C/rGO electrode indicated a larger Na^+ diffusion coefficient than VMC@C (Table S4, ESI†), which is ascribed to the enlarged surface area derived from the hierarchical structure. Electrochemical impedance spectroscopy (EIS) measurements of the VMC@C and VMC@C/rGO electrodes were acquired with fresh batteries and after ten cycles at 0.2C, respectively, to characterize the reaction kinetics of the Na^+ ions. The Nyquist plots and corresponding equivalent circuits are shown in Fig. 5a. Before cycling, both Nyquist plots are composed of a semicircle in the medium-high frequency region and a sloping line in the low frequency region. The semicircle represents the charge-transfer impedance (R_{ct}), corresponding to the sodium ion diffusion through the electrode–electrolyte interface, while the sloping line indicates the Warburg impedance of the sodium ion diffusion in the bulk of the electrode. In Table S5 (ESI†), it can be seen that the R_{ct} value of VMC@C/rGO (154 Ω) is lower than that of VMC@C (274 Ω). This result demonstrates that the highly conductive rGO networks can effectively improve the migration capability of sodium ions at the electrode–electrolyte interface. Impedance

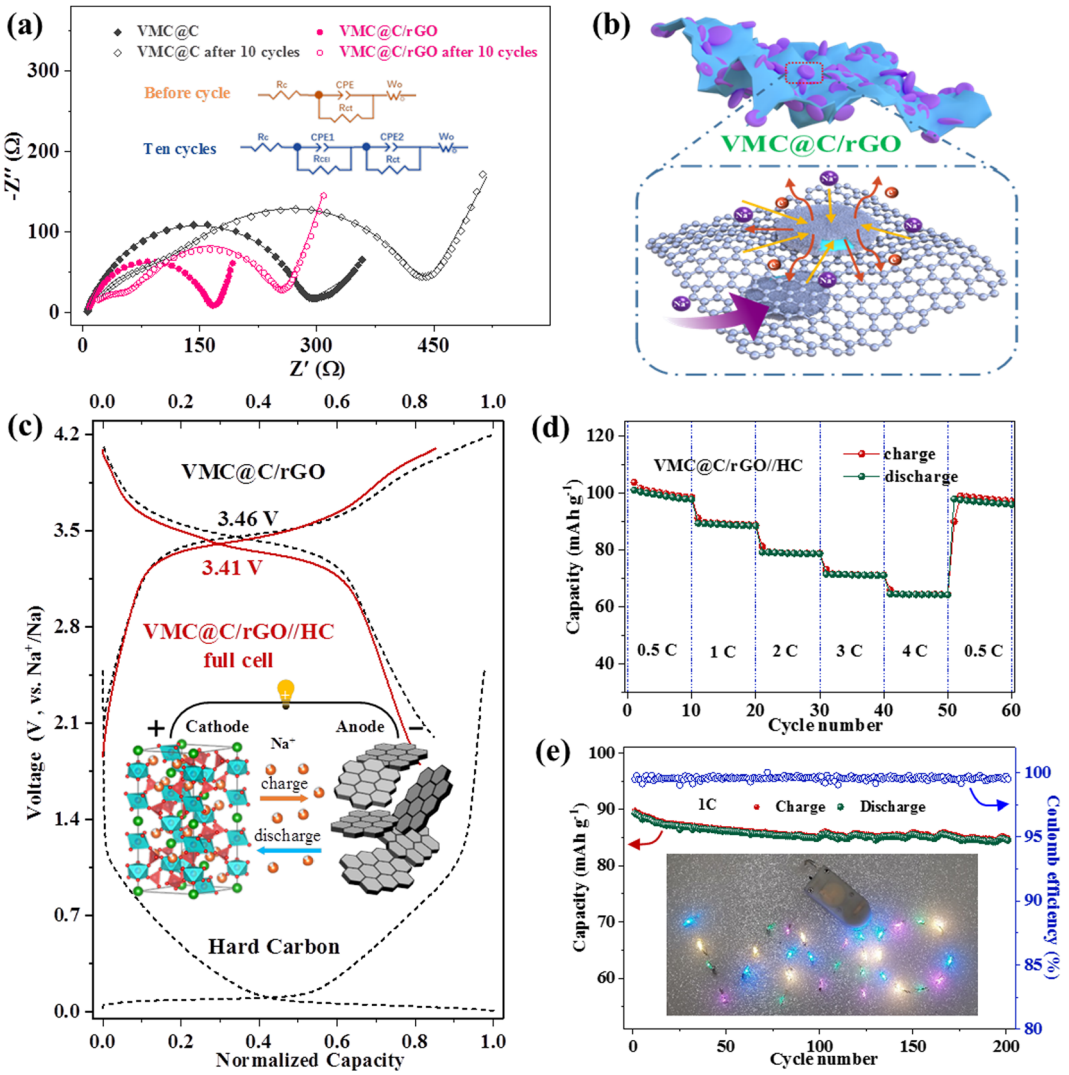

Fig. 5 (a) EIS spectra of VMC@C and VMC@C/rGO under fresh cell and after ten cycles at 0.2C; the insets are the equivalent circuit used to simulate the EIS spectra, and the lines represent fitting results. (b) Illustration of the transport paths of Na^+ ions and electrons of the VMC@C/rGO composite. (c) Charge–discharge curves of the VMC@C/rGO cathode, HC anode and VMC@C/rGO//HC full cell at 0.2C; inset is the schematic diagram of the VMC@C/rGO full cell. (d) Rate performance from 0.5 to 4C. (e) Cycle property of the VMC@C/rGO//HC full cell at 1C; inset is the digital image of lighting 30 LED lights for 'VMC' letters.

spectroscopy offers an alternative method to calculate the apparent diffusion coefficients by applying eqn (5):[61]

$$D_{Na^+} = R^2T^2/2n^2A^2C_o^2F^4\sigma_\omega^2 \quad (5)$$

where R is the gas constant, T is the absolute temperature, A is the geometrical electrode area, n is the electron transfer number in the electrochemical reaction, F is the Faraday's constant, and C_o is the concentration of Na^+. Eventually, the Warburg coefficient (σ_ω) can be determined as the slope of the linear behavior of the real impedance (Z') *versus* the reciprocal root square of low frequencies (Fig. S7, ESI†). The calculated sodium ion diffusion coefficients are 7.48×10^{-12} and 2.23×10^{-12} cm^2 s^{-1} of the VMC@C/rGO and VMC@C electrodes, respectively, suggesting faster Na^+ ion diffusion rate in VMC@C/rGO.[62] After ten cycles at 0.2C, the EIS spectra (Fig. 5a) comprise two semicircles, the high-frequency semicircle characterizing the resistance of the cathode electrolyte interphase (CEI) layer (R_{CEI}), and the medium frequency semicircle reflecting the charge transfer resistance (R_{ct}). This result reveals that the electrolyte decomposed in the high voltage range to form the CEI film, leading to the capacity decay (Fig. 3c).[63]

The excellent sodium storage properties of VNC@C/rGO, including high reversible capacity, stable cycling performance and remarkable rate capability, can be attributed to the following reasons and as illustrated in Fig. 5b. Firstly, the amorphous carbon tightly coated on surface of $Na_{3.5}VMn_{0.5}C_{r0.5}(PO_4)_3$ nanoparticles not only enhances the intrinsic electronic conductivity of $Na_{3.5}VMn_{0.5}Cr_{0.5}(PO_4)_3$, but also shortens the diffusion distance of sodium ions during the Na^+ insertion/de-insertion process.[64,65] Second, the rGO skeleton acts as a conductive array, resulting in improved electrochemical reactivity and reversibility. Third, this nanoparticles-on-channel

hierarchical structure not only affords a large the electrode/electrolyte contact area for the Na^+ ion diffusion and tunnel, but also provides adequate space as a Na^+ ion reservoir and for volume expansion during continuous charging/discharging. The V element also provides most of the capacity contribution. Mn not only provides part of the capacity, but also improves the working voltage.[39] Cr substitution could decrease the energy barriers for Na^+ ion migration and enhance the structural stability.[36,66] Lastly, benefiting from the reasonably designed hierarchical nanostructure and synergistic effect of the doping element, the VMC@C/rGO material exhibits excellent sodium storage properties.

To further evaluate the practicability of the VMC@C/rGO cathode material in SIBs, we fabricated the coin-type sodium ion full cell using HC as an anode material, written as VMC@C/rGO//HC, and shown in Fig. 5c. Before assembling the full cell, the HC anode first underwent three cycles to reduce the dramatic initial irreversible capacity loss. The cycle performance of the HC electrode from the fourth cycle is shown in Fig. S8 (ESI†). The electrochemical properties of the full cells were studied in the range of 1.8–4.1 V at room temperature. As shown in Fig. 5c, the VMC@C/rGO//HC full cell exhibits an operating potential of 3.41 V with the reversible capacity of 119 mA h g^{-1} at 0.2C, and consequential energy density of 405.8 W h kg^{-1}. Fig. 5d shows the rate capability of the VMC@C/rGO//HC full cell ranging from 0.5 to 4C. The obtained average specific capacities were 99.1, 88.8, 78.8, and 64.3 mA h g^{-1} at the rates of 0.5, 1, 2 3 and 4C, respectively. It can recover to 96.8 mA h g^{-1} when the rate returns to 0.5C. The lifespan of the full cell was evaluated under 1C (Fig. 5e). The reversible capacity is retained at 84.5 mA h g^{-1} after 200 cycles, corresponding to the capacity retention ratio of 94.6%, and the Coulombic efficiency is kept at above 99% during the whole cycling, indicating the excellent cycling stability of the VMC@C/rGO//HC full cell. Furthermore, two full cells connected in series can light up a 30 LED lights band in parallel with 'VMC' letters. Thus, our study confirms the potential of the hierarchical-structure $Na_{3.5}VMn_{0.5}Cr_{0.5}(PO_4)_3$ cathode for use in energy storage devices.

Conclusions

In summary, bivalent Mn and trivalent Cr element were explored to replace half of V in $Na_3V_2(PO_4)_3$ to design a new NASICON-type $Na_{3.5}VMn_{0.5}Cr_{0.5}(PO_4)_3$ cathode material. To overcome the drawback of inferior diffusion dynamics, a dual-carbon hierarchical $Na_{3.5}VMn_{0.5}Cr_{0.5}(PO_4)_3$@C/rGO material was successfully fabricated *via* a sol–gel procedure. Benefiting from the reasonably designed hierarchical nanostructure and synergistic effect, $Na_{3.5}VMn_{0.5}Cr_{0.5}(PO_4)_3$@C/rGO exhibits superior sodium storage capability. It can achieve a high energy density of 472 W h kg^{-1} at 0.2C, and a high capacity retention of 81% after 8000 cycles at 20C. The VMC@C/rGO//HC full cell also exhibits a high energy density of 405.8 W h kg^{-1} at 0.2C and excellent cycling stability (94.6% at 1C after 200 cycles). Furthermore, the nanoparticles-on-channel hierarchical-structure and cation substitution strategy illustrated in this work can be potentially applied to other high-performances NASIOCN-based cathode materials for SIBs.

Author contributions

Jinhao Wang: experiment, investigation, conceptualization, writing – original draft, funding acquisition. Longzhu Zhao: material preparation, investigation. Fengqi Lu: funding acquisition, conceptualization, writing – review &editing.

Conflicts of interest

There are no conflicts to declare.

Acknowledgements

This work was financially supported by the National Natural Science Foundation of China (No. 22269006), Guangxi Natural Science Foundation (No. 2020GXNSAA159005) and Guangxi BaGui Scholars Special Funding.

Notes and references

1 H. Li, M. Xu, Z. Zhang, Y. Lai and J. Ma, *Adv. Funct. Mater.*, 2020, **30**, 2000473.
2 C. Delmas, *Adv. Energy Mater.*, 2018, **8**, 1703137.
3 Y. You and A. Manthiram, *Adv. Energy Mater.*, 2017, **8**, 1701785.
4 J. Zhang, D. W. Wang, W. Lv, L. Qin, S. Niu, S. Zhang, T. Cao, F. Kang and Q. H. Yang, *Adv. Energy Mater.*, 2018, **8**, 1801361.
5 H. J. Liang, Z. Y. Gu, X. X. Zhao, J. Z. Guo, J. L. Yang, W. H. Li, B. Li, Z. M. Liu, W. L. Li and X. L. Wu, *Angew. Chem., Int. Ed.*, 2021, **60**, 26837–26846.
6 M.-S. Balogun, W. Qiu, W. Wang, P. Fang, X. Lu and Y. Tong, *J. Mater. Chem. A*, 2015, **3**, 1364–1387.
7 M. Thompson, Q. Xia, Z. Hu and X. S. Zhao, *Mater. Adv.*, 2021, **2**, 5881–5905.
8 G. L. Xu, R. Amine, A. Abouimrane, H. Che, M. Dahbi, Z. F. Ma, I. Saadoune, J. Alami, W. L. Mattis, F. Pan, Z. Chen and K. Amine, *Adv. Energy Mater.*, 2018, **8**, 1702403.
9 S. Chen, C. Wu, L. Shen, C. Zhu, Y. Huang, K. Xi, J. Maier and Y. Yu, *Adv. Mater.*, 2017, **29**, 1700431.
10 X. Yang and A. L. Rogach, *Adv. Energy Mater.*, 2020, **10**, 2000288.
11 G. Chen, Q. Huang, T. Wu and L. Lu, *Adv. Funct. Mater.*, 2020, **30**, 2001289.
12 X. Qiu, X. Wang, Y. He, J. Liang, K. Liang, B. L. Tardy, J. J. Richardson, M. Hu, H. Wu, Y. Zhang, O. J. Rojas, I. Manners and J. Guo, *Sci. Adv.*, 2021, **7**, eabh3482.
13 K. Wang, Z. Zhang, S. Cheng, X. Han, J. Fu, M. Sui and P. Yan, *eScience*, 2022, **2**, 529–536.

14 Q. Zhang, X. Shen, Q. Zhou, K. Li, F. Ding, Y. Lu, J. Zhao, L. Chen and Y.-S. Hu, *Energy Mater. Adv.*, 2022, **2022**, 9828020.
15 H. Gao, N. S. Grundish, Y. Zhao, A. Zhou and J. B. Goodenough, *Energy Mater. Adv.*, 2021, **2021**, 1932952.
16 Y. Fang, X.-Y. Yu and X. W. D. Lou, *Angew. Chem., Int. Ed.*, 2017, **56**, 5801–5805.
17 J. Qian, C. Wu, Y. Cao, Z. Ma, Y. Huang, X. Ai and H. Yang, *Adv. Energy Mater.*, 2018, **8**, 1702619.
18 Z. Jian, Y. S. Hu, X. Ji and W. Chen, *Adv. Mater.*, 2017, **29**, 1601925.
19 K. Chayambuka, G. Mulder, D. L. Danilov and P. H. L. Notten, *Adv. Energy Mater.*, 2018, **8**, 1800079.
20 Q. Liu, Z. Hu, M. Chen, C. Zou, H. Jin, S. Wang, S. L. Chou, Y. Liu and S. X. Dou, *Adv. Funct. Mater.*, 2020, **30**, 1909530.
21 M. Li, Z. Du, M. A. Khaleel and I. Belharouak, *Energy Storage Mater.*, 2020, **25**, 520–536.
22 T. Wang, D. Su, D. Shanmukaraj, T. Rojo, M. Armand and G. Wang, *Electrochem. Energy Rev.*, 2018, **1**, 200–237.
23 W. Song, X. Cao, Z. Wu, J. Chen, K. Huangfu, X. Wang, Y. Huang and X. Ji, *Phys. Chem. Chem. Phys.*, 2014, **16**, 17681–17687.
24 T. Wei, G. Yang and C. Wang, *Nano Energy*, 2017, **39**, 363–370.
25 S. Li, P. Ge, C. Zhang, W. Sun, H. Hou and X. Ji, *J. Power Sources*, 2017, **366**, 249–258.
26 Z. Yang, G. Li, J. Sun, L. Xie, Y. Jiang, Y. Huang and S. Chen, *Energy Storage Mater.*, 2020, **25**, 724–730.
27 X.-X. Zhao, Z.-Y. Gu, J.-Z. Guo, C.-D. Zhao, X.-T. Wang, D. Xie, W.-H. Li and X.-L. Wu, *Mater. Chem. Front.*, 2021, **5**, 5671–5678.
28 Q. Wang, H. Gao, J. Li, G. B. Liu and H. Jin, *ACS Appl. Mater. Interfaces*, 2021, **13**, 14312–14320.
29 L. Zhu, Q. Zhang, D. Sun, Q. Wang, N. Weng, Y. Tang and H. Wang, *Mater. Chem. Front.*, 2020, **4**, 2932–2942.
30 S. Ghosh, N. Barman, M. Mazumder, S. K. Pati, G. Rousse and P. Senguttuvan, *Adv. Energy Mater.*, 2019, **10**, 1902918.
31 C. Xu, J. Zhao, E. Wang, X. Liu, X. Shen, X. Rong, Q. Zheng, G. Ren, N. Zhang, X. Liu, X. Guo, C. Yang, H. Liu, B. Zhong and Y. S. Hu, *Adv. Energy Mater.*, 2021, **11**, 2100729.
32 F. Lu, J. Wang, S. Chang, L. He, M. Tang, Q. Wei, S. Mo and X. Kuang, *Carbon*, 2022, **196**, 562–572.
33 T. Zhu, P. Hu, X. Wang, Z. Liu, W. Luo, K. A. Owusu, W. Cao, C. Shi, J. Li, L. Zhou and L. Mai, *Adv. Energy Mater.*, 2019, **9**, 1803436.
34 H. Gao, Y. Li, K. Park and J. B. Goodenough, *Chem. Mater.*, 2016, **28**, 6553–6559.
35 M. Hadouchi, N. Yaqoob, P. Kaghazchi, M. Tang, J. Liu, P. Sang, Y. Fu, Y. Huang and J. Ma, *Energy Storage Mater.*, 2021, **35**, 192–202.
36 M. Chen, W. Hua, J. Xiao, J. Zhang, V. W. Lau, M. Park, G. H. Lee, S. Lee, W. Wang, J. Peng, L. Fang, L. Zhou, C. K. Chang, Y. Yamauchi, S. Chou and Y. M. Kang, *J. Am. Chem. Soc.*, 2021, **143**, 18091–18102.
37 J. Liu, K. Lin, Y. Zhao, Y. Zhou, X. Hou, X. Liu, H. Lou, K.-H. Lam and F. Chen, *J. Mater. Chem. A*, 2021, **9**, 10437–10446.
38 S. Ghosh, N. Barman and P. Senguttuvan, *Small*, 2020, **16**, e2003973.
39 W. Zhou, L. Xue, X. Lu, H. Gao, Y. Li, S. Xin, G. Fu, Z. Cui, Y. Zhu and J. B. Goodenough, *Nano Lett.*, 2016, **16**, 7836–7841.
40 J. Zhang, Y. Liu, X. Zhao, L. He, H. Liu, Y. Song, S. Sun, Q. Li, X. Xing and J. Chen, *Adv. Mater.*, 2020, **32**, e1906348.
41 P. Lavela, R. Klee and J. L. Tirado, *J. Power Sources*, 2021, **495**, 229811.
42 W. S. Hummers Jr and R. E. Offeman, *J. Am. Chem. Soc.*, 1958, **80**, 1339.
43 Y. Fang, L. Xiao, X. Ai, Y. Cao and H. Yang, *Adv. Mater.*, 2015, **27**, 5895–5900.
44 Y. Zhou, X. Shao, K. H. Lam, Y. Zheng, L. Zhao, K. Wang, J. Zhao, F. Chen and X. Hou, *ACS Appl. Mater. Interfaces*, 2020, **12**, 30328–30335.
45 C. Xu, J. Zhao, Y. A. Wang, W. Hua, Q. fu, X. Liang, X. Rong, Q. Zhang, X. Guo, C. Yang, H. Liu, B. Zhong and Y. S. Hu, *Adv. Energy Mater.*, 2022, **12**, 2200966.
46 Z. Zhang, Z. Chen, Z. Mai, K. Peng, Q. Deng, A. Bayaguud, P. Zhao, Y. Fu, Y. Yu and C. Zhu, *Small*, 2019, **15**, e1900356.
47 T. Zhu, P. Hu, C. Cai, Z. Liu, G. Hu, Q. Kuang, L. Mai and L. Zhou, *Nano Energy*, 2020, **70**, 104548.
48 Y. Chen, J. Cheng, S. Sun, Z. Tian, X. Jiang, Y. Wang, Z. He, C. Liu, Q. Huang and L. Guo, *J. Power Sources*, 2021, **513**, 230545.
49 N. S. Buryak, D. V. Anishchenko, E. E. Levin, S. V. Ryazantsev, V. Martin-Diaconescu, M. V. Zakharkin, V. A. Nikitina and E. V. Antipov, *J. Power Sources*, 2022, **518**, 230769.
50 F. Li, Y.-E. Zhu, J. Sheng, L. Yang, Y. Zhang and Z. Zhou, *J. Mater. Chem. A*, 2017, **5**, 25276–25281.
51 R. Klee, P. Lavela and J. L. Tirado, *Electrochim. Acta*, 2021, **375**, 137982.
52 Zelang Jian, Liang Zhao, Huilin Pan, Yong-Sheng Hu, Hong Li, Wen Chen and L. Chen, *Electrochem. Commun.*, 2012, **14**, 86–89.
53 X. Pu, D. Zhao, C. Fu, Z. Chen, S. Cao, C. Wang and Y. Cao, *Angew. Chem., Int. Ed.*, 2021, **60**, 21310–21318.
54 Y. Jiang, Z. Yang, W. Li, L. Zeng, F. Pan, M. Wang, X. Wei, G. Hu, L. Gu and Y. Yu, *Adv. Energy Mater.*, 2015, **5**, 1402104.
55 L. Zhao, X. Rong, Y. Niu, R. Xu, T. Zhang, T. Li, Y. Yu and Y. Hou, *Small*, 2020, **16**, e2004925.
56 H. Li, M. Xu, C. Gao, W. Zhang, Z. Zhang, Y. Lai and L. Jiao, *Energy Storage Mater.*, 2020, **26**, 325–333.
57 H. Li, T. Jin, X. Chen, Y. Lai, Z. Zhang, W. Bao and L. Jiao, *Adv. Energy Mater.*, 2018, **8**, 1801418.
58 M. Chen, W. Hua, J. Xiao, D. Cortie, W. Chen, E. Wang, Z. Hu, Q. Gu, X. Wang, S. Indris, S. L. Chou and S. X. Dou, *Nat. Commun.*, 2019, **10**, 1480.
59 R. Zhan, B. Shen, Q. Xu, Y. Zhang, Y. Luo, H. Liu, H. Chen, F. Liu, C. Li and M. Xu, *Electrochim. Acta*, 2018, **283**, 1475–1481.
60 M. Peng, D. Zhang, L. Zheng, X. Wang, Y. Lin, D. Xia, Y. Sun and G. Guo, *Nano Energy*, 2017, **31**, 64–73.
61 X. H. Rui, N. Ding, J. Liu, C. Li and C. H. Chen, *Electrochim. Acta*, 2010, **55**, 2384–2390.

62 J. Wang, X. Li, Z. Wang, H. Guo, B. Huang, Z. Wang and G. Yan, *J. Solid State Electrochem.*, 2014, **19**, 153–160.
63 C. Xu, R. Xiao, J. Zhao, F. Ding, Y. Yang, X. Rong, X. Guo, C. Yang, H. Liu, B. Zhong and Y.-S. Hu, *ACS Energy Lett.*, 2021, **7**, 97–107.
64 X. Zhang, M. Yu, S. Zhao, F. Li, X. Hu, S. Guo, X. Lu and Y. Tong, *Part. Part. Syst. Charact.*, 2016, **33**, 531–537.
65 Y. Fang, X.-Y. Yu and X. W. Lou, *Matter*, 2019, **1**, 90–114.
66 H. Yu, X. Ruan, J. Wang, Z. Gu, Q. Liang, J. M. Cao, J. Kang, C. F. Du and X. L. Wu, *ACS Nano*, 2022, **16**, 21174–21185.